



Control of surface acidity and catalytic activity of γ -Al₂O₃ by adjusting the nanocrystalline contact interface

Roxana Vidruk^a, Miron V. Landau^{a,*}, Moti Herskowitz^a, Vladimir Ezersky^b, Amir Goldbourt^c

^a Blechner Center for Applied Catalysis and Process Development, Department of Chemical Engineering, Ben-Gurion University of the Negev, Beer-Sheva 84105, Israel

^b Department of Materials Engineering, Ben-Gurion University of the Negev, Beer-Sheva 84105, Israel

^c School of Chemistry, Raymond and Beverly Sacker, Faculty of Exact Sciences, Tel-Aviv University, Ramat Aviv, Israel

ARTICLE INFO

Article history:

Received 28 March 2011

Revised 29 May 2011

Accepted 15 June 2011

Available online 22 July 2011

Keywords:

Aluminum oxide

Acidity

Nanoparticles contact interface

Densification

Isopropanol dehydration

ABSTRACT

Densification of 2–2.5 nm nanocrystals assemblies in the three-level hierarchical structure of γ -Al₂O₃ aerogel significantly increases the surface acidity, as determined using indicator titration, NH₃-TPD, and FTIR of adsorbed pyridine. Thermal treatment at 1073 K and insertion of additional alumina inside the aerogel pores eliminated the slit micropores with shrinkage of nanocrystals assemblies (N₂-adsorption, HRTEM, SEM) increasing the contact interface by a factor of 2. It caused a fivefold increase in alumina surface acidity and the strength of Lewis acid sites with no measurable dehydration (weight loss, TGA). This was attributed to the formation of additional low-coordinated aluminum ions with higher charge in the areas with atomic disorder of high-angle grain boundaries, detected by ²⁷Al MAS NMR, HRTEM, XPS, and XRD. Densification of nanocrystalline alumina aerogel yielded a higher catalytic activity in dehydration of isopropanol; it was 10-fold more active compared with commercial γ -alumina on the catalyst weight basis.

© 2011 Elsevier Inc. All rights reserved.

1. Introduction

Advanced solid catalytic materials have structures that are organized at the nanoscale with hierarchical porosity [1]. For these materials, the nonporous nanocrystals of the catalytic phases (metals, metal oxides, mixed oxides, etc.) and the porous matrices stabilizing them (silica, alumina titania, etc.) are prepared and combined by special methods designed to decrease the particle size and minimize the screening of catalytic phases thereby yielding the highest possible accessible surface area [1,2]. From this point of view, the contact interface between the nanoparticles in the catalytic material should be minimized, but sometimes contact between the nanoparticles enhances catalytic performance. In the latter case, it is necessary to compensate for the decrease in the accessible surface area with other factors that significantly enhance the catalytic activity. The extent of this “pay-off” will depend on the structure and catalytic functionality of the nanoparticles, which differ for multi-phase and monophase catalysts.

In multiphase catalysts, the contact interface brings together the different chemical functionalities of the catalytic phases and/or strengthens the catalytic phase-support interactions. According to the “extended perimeter” hypothesis of Haruta and co-workers

[3] – as later confirmed by Rolison and co-workers [4] – the formation of multiple junctions between Au and TiO₂ nanoparticles in Au/TiO₂ catalysts increases the CO oxidative turnover shortening the average lateral diffusion distance of CO adsorbed on gold to the oxygen-activating Au–TiO₂ interface. Similar effects were observed in other catalytic reactions using multiphase nanocomposite catalysts; for example, carbon dioxide reforming of methane to syngas with NiO–CeZrO_x [5], oxidation of isobutene to methacrolein with FeSbO₄– α Sb₂O₄ [6], and hydrogenation of benzene with sandwiched Ru-carbon nanostructures [7]. In these examples, the formation of an interface between nanoparticles constituting different phases provided three-dimensional control of the reaction zone, thereby improving the contact between the spillover source and the secondary catalytic receptor.

The contact interface between nanoparticles also plays a significant role in the performance of electrochemically promoted catalysts [8], including chemical sensors whose sensitivity is controlled by the resistance of metal (Pt, Pd)–semiconductor (SnO₂, In₂O₃) composites [9,10]. In multiphase catalytic materials, the nanoparticle interface can be engineered to control the state of the surface atoms involved in the catalytic cycles. This may be achieved via two mechanisms – electronic interaction by interfacial charge distribution or chemical interaction by interfacial atom transport, leading to the formation of compounds with novel chemical properties [11,12].

* Corresponding author. Fax: +972 8 6479427.

E-mail address: mlandau@bgu.ac.il (M.V. Landau).

In monophasic catalytic materials, the reactivity of nanoparticles with the same chemical functionality, i.e., metals or ionic crystals such as individual or mixed metal oxide phases, is changed in the vicinity of contact interface due to interfacial atom transport. In many organic reactions, the catalytic activity of metal nanoparticles and inorganic ionic nanocrystals is determined by low-coordinated surface atoms or ions [13]. Areas of atomic disorder formed at the interface of crystal grains – grain boundaries (GB) – were theoretically predicted to be a source of low-coordinated active sites in solid catalysts [14]. The stabilization of atomic disorder arising in these areas as a result of the counter-current atoms/ions/vacancies diffusion through the interface of nanocrystals with mismatch of atomic layers was confirmed by more accurate density functional theory (DFT) calculations [15–17] and by experimental observations [15,16,18–21]. Several groups attributed the observed catalytic effects to the modified space of the “active zone” – GBs around the nanocrystals contact interface in monophasic nanocrystalline catalytic materials. In these studies, the “active zone” was altered by changing the preparation strategy of the catalysts or varying the loading of the catalytic phase on the support. Kalyaguine and co-workers ascribed the high oxygen mobility that controlled the catalytic activity of perovskites in methane oxidation to rapid diffusion of activated oxygen species along the GBs [22,23]. Kiely and co-workers proved that GBs (formed when disoriented MgO nanocrystals impinge on each other) constituted charged regions attracting lithium ions that formed $[\text{Li}^+\text{O}^-]$ sites for oxidative coupling of methane [24–26]. Tsybulya and co-workers demonstrated that defects formed at the inter-grain boundaries of silver nanocrystals led the catalytic activity in ethylene epoxidation [27]. The inter-grain disordered regions, whose formation decreased the surface area of Pt- and Pt–Ru catalysts, were considered by Kapolskii and co-workers as a source of increased catalytic activity in the electro-oxidation of methanol [28].

However, experimental implementation of low-coordinated sites in GB areas of ionic crystals has been hampered by the lack of techniques for controlled formation of GB in such nanocrystalline solids. Landau and co-workers recently demonstrated that the surface chemical functionality, i.e., the surface basicity, of ionic MgO nanocrystal assemblies and their catalytic activity, could be controlled by quantitative alteration of the nanocrystal interface by using chemical or pressure-assisted densification of a magnesia aerogel [29]. Areas with atomic disorder were also found at the GBs of nanostructured γ -alumina [30] that is known as a catalytic material with acidic functionality that is effective as a solid Lewis acid in many organic reactions of practical importance [31,32]. Atomic disorder in GB areas stabilizes aluminum ions with fewer oxygen in the first coordination sphere compared with regular bulk structure, thereby creating low-coordinated aluminum as Lewis acid sites. The present work demonstrated that the surface acidity and catalytic activity of nanocrystalline γ -alumina in the dehydration of isopropanol – a catalytic reaction used as an indicator of the type and strength of acid sites [33] – can be controlled over a wide range by altering the interface of the primary nanocrystals. To clarify the origin of this phenomena, the friable packing of primary γ -alumina nanocrystals in starting aggregates (green compacts) was changed to dense packing increasing the contact interface between nanoparticles that facilitates the formation of GB – areas with ionic disorder. Densification of green compacts and creation of GB was proven by N_2 -adsorption, HRTEM, XRD, and ^{27}Al MAS NMR, while its effect on the surface chemical functionality of alumina was tested by characterization of surface acidity by indicator titration, NH_3 -TPD, FTIR of adsorbed pyridine and catalytic performance. In this study, chemical and thermal densification of alumina aerogel was applied to increase the concentration of low-coordinated aluminum ions.

2. Experimental

2.1. Catalyst preparation

2.1.1. Alumina aerogel

The oxide–hydroxide AIOOH gel precursor of γ - Al_2O_3 was prepared by sol–gel processing according to the procedure reported in [34]. The obtained gel was dried by supercritical solvent release; 7.04 g of aluminum *sec*-butoxide (Aldrich) was dissolved in 60 ml of EtOH (BioLab) at 353 K and partially hydrolyzed with solution of 0.22 g water/40 ml EtOH/0.11 g nitric acid (69 wt.%). After 2 h of stirring, a clear alumina sol was formed. The solution was cooled to room temperature, and 0.57 g of water diluted with 5 ml EtOH was added, leading to the formation of a bulk gel. The wet gel was allowed to age overnight and then placed in a glass vessel inside an autoclave; 50 ml of EtOH was also placed in the autoclave next to the glass vessel. The autoclave was then purged with nitrogen, and the temperature was increased to 543 K at 1 K min^{-1} up to 90 bar. After 10 min, the pressure was decreased slowly at constant temperature to allow supercritical solvent release. To obtain crystalline aluminum oxide (A-1073-2), the AIOOH aerogel precursor obtained as described above was calcined in a tube furnace under a flow of helium at 573 K for 2 h and then under a flow of oxygen at 1073 K for 2 h.

Thermal densification of the γ - Al_2O_3 aerogel, designated A-1073-2, so obtained was conducted by further heating of this material at 1073 K for 4 h (A-1073-6), 8 h (A-1073-10) or 12 h (A-1073-14) in air. “Chemical densification” was carried out by incipient wetness impregnation of the supercritically dried aluminum oxide–hydroxide aerogel precursor with an aqueous solution of $\text{Al}(\text{NO}_3)_3$ (Fluka) at 45 wt.% Al_2O_3 loading relative to the alumina content in the aerogel. The alumina aerogel after supercritical drying was evacuated in the rotavapor under residual pressure of 20 mbar that facilitated insertion of aluminum nitrate salt inside the aerogel pores. At room temperature, to this material was dropwise added aqueous solution of aluminum nitrate (0.75 mol l^{-1} ; pH = 1.4) at amount of 10.5 ml g^{-1} . The chemically densified alumina aerogel (designated ACD-1073-2) was obtained by drying of the impregnated material in air at 393 K for 18 h, followed by calcination in two steps (in He at 573 K for 2 h and then in O_2 at 1073 K for 2 h) under the same conditions as those used in the preparation of the starting aerogel precursor.

2.1.2. Alumina xerogel

The γ - Al_2O_3 xerogel (X-823-3) was prepared according to the procedure reported in [35] by precipitation from aqueous solution of $\text{Al}(\text{NO}_3)_3$; 11.03 g $\text{Al}(\text{NO}_3)_3 \cdot 9\text{H}_2\text{O}$ was dissolved in 30 ml H_2O . The gelation was achieved by addition of ammonium hydroxide solution and adjusting solution pH to 10. The gel was washed with water and isopropanol, separated from the washing liquid by filtration, and then heated in air to 823 K at a heating rate of 5 K min^{-1} and maintained at this temperature for 3 h.

2.1.3. Reference commercial aluminas

For comparison, three commercial γ - Al_2O_3 materials were tested: C1-823-2 (Norton SA 6176 1/8" extruded; S.A. = $235 \text{ m}^2 \text{ g}^{-1}$), C2-823-2 (Norton XA 08222 1/8" rings; S.A. = $153 \text{ m}^2 \text{ g}^{-1}$), and C3-823-2 (Engelhard Al0104T 1/8" extruded; S.A. = $106 \text{ m}^2 \text{ g}^{-1}$). All studied commercial catalysts were crushed into powder (fraction 99–425 μm or 150–40 mesh) and treated for 2 h at 823 K in He. Loss on ignition of the samples was in range of 3–4 wt.%.

2.1.4. Catalysts labels

The labeling of materials in Sections 2.1.1–2.1.3, and in the following description, discussion of experimental data were done in a

uniform way. The prepared alumina catalytic materials were labeled starting from definition of samples origin: A – aerogel, ACD – aerogel chemically densified, X – xerogel, and C – commercial samples, followed by abbreviations reflecting their thermal treatment history – temperature and duration. That is, aerogel treated at 1073 K for 2 h was denoted as A-1073-2, original commercial materials treated at 823 K for 2 h – C1-823-2 to C3-823-2, and xerogel treated at 823 K for 3 h – X-823-3.

2.2. Catalyst characterization

Surface area, pore volume, and pore size distribution were derived from N₂ adsorption–desorption isotherms, by using conventional BET and BJH methods. The micropore volume and surface area were derived from the adsorption branch of the isotherm by using the *t*-plot method. The samples were outgassed under vacuum for 2 h at 523 K, and isotherms were obtained on a NOVA-2000 (Quantachrome, Version 7.02) instrument at the temperature of liquid nitrogen.

Conventional wide-angle XRD patterns were obtained with a Philips 1050/70 powder diffractometer fitted with a graphite monochromator, at 40 kV and 28 mA. Software developed by Crystal Logic was used. The data were collected in a range of 2θ values between 5° and 80° with a step size of 0.05°. Phase identification was performed by using BEDE ZDS computer search/match program coupled with the ICDD (International Center for Diffraction Data) Powder Diffraction File database (2006). The γ -Al₂O₃ crystal size was determined from the Scherrer equation $h = K\lambda/[(B^2 - \beta^2)^{0.5} \cos(2\theta/2)]$, where $K = 1.000$ is the shape factor, $\lambda = 0.154$ nm, β is the instrumental broadening correction, and B is the reflection broadening at corresponding 2θ . The average crystal size was obtained by averaging of the data calculated for reflections (1 1 1), (2 2 0), (3 1 1), (3 2 2), (4 0 0), (5 1 1), and (4 4 0) of the XRD patterns corresponding to the cubic γ -Al₂O₃ phase (ICDD Card 79-1558).

Differential (DTA) and gravimetric (TGA) thermal analyses were done over a temperature range from room temperature to 1073 K with a TG-50-Mettler-Toledo instrument. The measurements were carried out in a flow of air at a heating rate of 5 K min⁻¹.

Single-pulse²⁷Al magic angle spinning solid-state NMR experiments were performed with a pulse length of 2 μ s, a radio frequency (RF) of 50 kHz, a repetition rate of 0.5 s, and a spinning rate of 14.9 kHz. A solution of 1 M AlCl₃ was used as a reference at 0 ppm and to determine the RF power level. Proton decoupling had no detectable impact on the spectra and was therefore not used. ²⁷Al spectra were measured using a 4-mm probe on a 600WB Bruker Avance-III spectrometer operating at a ²⁷Al Larmor frequency of 156.4 MHz.

SEM micrographs were obtained on Quanta-200, SEM-EDAX, FEI Co. instrument. The samples were covered with gold to prevent surface charging. HRTEM analysis was conducted on a FasTEM JEOL 2010 microscope operating at 200 kV. The samples for HRTEM were prepared by depositing a drop of ethanol suspension of the solid catalyst on a carbon-coated copper grid.

The concentration of surface acid sites was determined by titration with methyl red, 0.05 g in 30 ml of toluene, as the indicator [36]. A suspension of 30 mg of γ -Al₂O₃ in 5 ml toluene after addition of indicator solution was stirred for 3 h at room temperature and then titrated against a 0.05 M solution of *n*-butylamine in toluene. The results were expressed as surface acidity per gram alumina. The surface acidity of the obtained γ -Al₂O₃ samples was also characterized by TPD of preadsorbed NH₃. The experiments were performed in AMI-100 Catalyst Characterization System (Zeton-Altamira), equipped with a mass-spectrometer (Ametek 1000) for identification of components in the outlet gas. γ -Al₂O₃ (0.2 g) was calcined at 823 K for 2 h and then cooled in a He flow. The samples were then saturated with 5 vol.% NH₃/He at 303 K, purged

with He to remove physically adsorbed NH₃, and heated in a He flow at 10 K min⁻¹. The integral intensity of the TPD peaks corresponding to mass 17 (NH₃) indicated the amount of acidic sites, while the positions of desorption peaks indicated the acidic strength.

The nature of pyridine moieties chemisorbed at the surface of γ -Al₂O₃ materials was determined by Fourier transform infrared spectroscopy (FTIR). Before analysis, the γ -Al₂O₃ samples were calcined at 823 K in He, cooled to room temperature, exposed for 1 h to a stream of saturated pyridine vapor in He at 423 K, and finally treated with pure He for 15 min to remove the physically adsorbed pyridine. The infrared spectra of samples prepared in KBr pellets (0.005 g sample and 0.095 g KBr) without contacting with ambient atmosphere were recorded on a Nicolet Impact 460 FTIR spectrometer, with 32 sample scans, at room temperature with outgassing treatment. The data were treated with OMNIC software.

XPS spectra were measured with ESCALAB 250 ultra-high vacuum (13×10^{-13} bar) apparatus with an Al K α X-ray source and a monochromator. Powder samples of the catalysts were pressed into a thin layer on an indium-plated grid. The spectral components of O and Al signals were found by fitting a sum of single-component lines to the experimental data by means of nonlinear least-squares curve fitting. The single-component lines were assumed to have the shape of the sum of Cauchy and Gaussian curves, and deconvolution was performed. To correct for charging effects, all spectra were calibrated relative to a carbon 1s peak positioned at 285.0 eV.

2.3. Catalytic activity in the dehydration of isopropanol

Dehydration of isopropanol was performed in fixed bed flow reactor at 523 K. Catalyst granules (300–600 μ m) were prepared by pelletizing the catalyst powder and crushing the pellets to the size desired for excluding the internal diffusion limitations. Prior to reaction, the catalysts were activated in flow of He at 823 K for 1.5 h. The isopropanol was fed with an HPLC pump to the tubular preheater where it was mixed with He and heated to the reaction temperature prior entering to the reactor. The weight hour space velocity (WHSV) was varied in the range of 5–10 h⁻¹ so as to keep the isopropanol conversion $x < 25\%$, i.e., to enable us to work in a differential reactor mode. The liquid products – water, acetone, di-isopropyl ether, and unreacted isopropanol – were collected in a cooled container (258 K) and analyzed in a Varian 3300 gas chromatograph, equipped with a thermal conductivity detector (TCD) and Poropack Q packed column (6 ft, 1/8 in., i.d. 3 mm), with He as the carrier gas. The standard calibration curves for water, acetone, di-isopropyl ether, and isopropanol were obtained using acetonitrile as an internal standard. The reaction rate normalized per 1 g and 1 m² of catalyst was calculated according to equations:

$$Rate_w [\text{mmol g}^{-1} \text{h}^{-1}] = \text{WHSV}x/Mw$$

$$Rate_s [\text{mmol m}^{-2} \text{h}^{-1}] = \text{WHSV}x/MwS.A._{BET}$$

$$\text{TOF} [\text{h}^{-1}] = \text{Rate}_w/[A]$$

where x – isopropanol conversion, Mw – the molecular weight of isopropanol, $S.A._{BET}$ – catalyst surface area, and $[A]$ – concentration of acidic sites (mmol g⁻¹).

3. Results and discussion

3.1. Structure and texture of parent and densified alumina aerogels

The alumina aerogel A-1073-2 (synthesized by using a sol–gel strategy followed by supercritical drying of obtained gel) was calcined first in He at 573 K for 2 h and then in pure O₂ at 1073 K for 2 h, the O₂ treatment being required for complete crystallization of

the γ - Al_2O_3 phase from aluminum oxide-hydroxide [33]. Comparison of the XRD patterns of the starting and calcined aerogels (Fig. 1, curves 1 and 2) confirmed the full conversion of partially hydrated AlOOH precursor [whose structure comprised a mixture of three phases AlOOH , $\text{AlO}(\text{OH})$, and $(\text{Al}_2\text{O}_3)_{11}(\text{H}_2\text{O})_{1.79}$ (ICDD Cards ## 48-890, 49-133, and 70-384, respectively)] into a highly dispersed material with a well-defined γ - Al_2O_3 structure (ICDD Card 79-1558) containing traces of an amorphous AlO_x phase (halo at $2\theta = 30^\circ$), in agreement with [34]. The obtained alumina oxide A-1073-2 was used as a reference alumina aerogel whose properties – structure, texture, surface acidity, and catalytic performance – were compared with those of densified alumina aerogels and commercial aluminas.

The packing of nanoparticles in green compacts like alumina is characterized by the fact that they produce a two-level hierarchical porous structure [37–39]. Such compacts are invariably made up of microporous agglomerates 10–30 times larger than the primary nanoparticle. Packing of the agglomerates forms secondary mesoporous aggregates that are tens of microns in size constituting the materials powder. The reference alumina aerogel was a powder with a relatively wide particle size distribution in the range of 1–50 μm , as shown by SEM micrographs recorded at a magnification of $3\text{--}5 \times 10^3$, at which intraparticle (aggregates) pores cannot be observed (Fig. 2a). Increasing the magnification up to 1×10^5 demonstrated that these micron-sized particles are made up of smaller elongated nanoparticles 25–100 nm in size with interparticle voids representing pores of 20–100 nm size (Fig. 2b). Further information about the structure of these smaller nanoparticles was obtained by HRTEM. The HRTEM micrograph of the reference aerogel (Fig. 3a) demonstrated that the 25–100 nm particles are made up of primary 2–3 nm nanocrystals of near-globular form, separated by 0.3- to 0.7-nm slit shape micropores (inset in Fig. 3a). Some, but not all, of these nanocrystals observed in the HRTEM

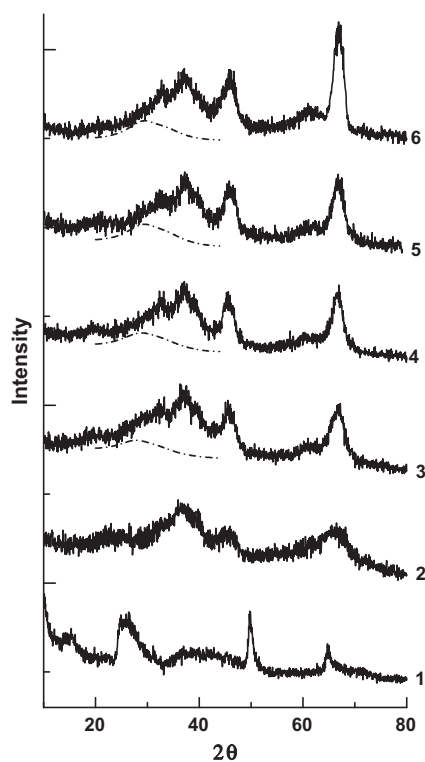


Fig. 1. X-ray diffraction patterns of alumina aerogel precursor (1) and γ - Al_2O_3 materials derived from this aerogel: (2) A-1073-2; (3) A-1073-6; (4) A-1073-10; (5) A-1073-14; and (6) ACD-1073-2.

micrographs displayed parallel fringes, reflecting atomic layers in the γ - Al_2O_3 . The parallel fringes across the nanoparticle images (Fig. 3d) have a periodicity of 2.4 \AA , which corresponds to planes (3 1 1) with d -spacings equal to $d_{311} = 2.398 \text{ \AA}$ in the cubic γ - Al_2O_3 structure. Many, but not all nanocrystals, were split by clearly visible slit pores. Changing the orientation of the sample relative to the electron beam by tilting it at angles of $\pm 10^\circ$ revealed novel nanocrystals with detectable fringes of atomic layers and slit pores. These findings constituted evidence for the high crystallinity of the material, in agreement with the X-ray diffraction data and the uniform spatial distribution of the micropores in aggregates of primary nanocrystals. The size of the primary γ - Al_2O_3 nanocrystals of 2–3 nm observed in HRTEM micrographs of the reference aerogel was in complete agreement with the size of the domains of coherent scattering derived from the broadening of X-ray diffraction peaks. This agreement confirms the origin of the particles of intermediate size as nanocrystal agglomerates.

The N_2 adsorption–desorption isotherms for the reference aerogel (Fig. 4a) are consistent with its micro-mesoporous structure that was deduced from the microscope studies. With a H1 shape of the hysteresis loop, these isotherms are characteristic of mesoporous materials with a relatively small contribution of microporosity to the pore volume. The reference aerogel displayed a high total surface area of $498 \text{ m}^2 \text{ g}^{-1}$ and a wide pore size distribution in the range of 10–90 nm (Fig. 4b), corresponding to a total pore volume of $3.5 \text{ cm}^3 \text{ g}^{-1}$ (Table 1). The contributions of micropores to the total surface area and pore volume were $43 \text{ m}^2 \text{ g}^{-1}$ and $1.9 \times 10^{-2} \text{ cm}^3 \text{ g}^{-1}$, respectively. The aggregation ratio of the primary nanocrystals was calculated according to equation [23,29]:

$$\Psi = S.A._{\text{theor}}/S.A._{\text{BET}},$$

where S.A. – surface area ($\text{m}^2 \text{ g}^{-1}$), D – average particle size (nm) derived from X-ray diffraction data, $S.A._{\text{theor}} = 6000/(\rho_{\gamma\text{-Al}_2\text{O}_3} * D)$ – theoretical surface area for particles of spherical or cubic shape, and $\rho_{\gamma\text{-Al}_2\text{O}_3} = 3.65 \text{ g cm}^{-3}$, the theoretical density of the γ - Al_2O_3 phase. The model considers nanoparticles as cubes with edge length D approximating the faceted shape of globular primary nanocrystals of γ - Al_2O_3 observed by HRTEM (Fig. 3a). The obtained value of the aggregation ratio $\Psi = 1.7$ (Table 1) is evidence of the friable packing of the primary nanocrystals in the intermediate particles – aggregates. Assuming dense packing face-to-face of cubic particles, the value of $\Psi = 1.7$ indicates that the interface's share of the total nanocrystal surface is about 40%. This value points out that there is significant potential for further densification of the material.

The treatment of the aerogel was designed so as to increase the contact interface between primary γ - Al_2O_3 nanocrystals as a precondition for increasing the GB areas by countercurrent diffusion of atoms/ions/vacancies. This treatment was designed to enhance inter-agglomerate densification (shrinkage of the primary nanocrystal aggregates) to eliminate micropores rather than to stimulate the intra-agglomerate densification that eliminates mesopores. The importance of mesopores lies in their ability to maximize porosity and surface area of the densified catalytic material. Sintering of the nanocrystals increases their size, and γ - α phase transition leads to the formation of micropores due to the higher theoretical density of α - Al_2O_3 phase. Increasing the crystal size and formation of micropores decrease the nanocrystals contact interface and GB areas, while α - Al_2O_3 is a catalytically inert phase. Densification and sintering of nanocrystalline ceramic oxide powders have been discussed in several comprehensive reviews [40–43]. Based on theoretical considerations, the defined target can be achieved by implementing low-temperature pressureless techniques to eliminate the micropores by vacancy diffusion along the GBs at relatively low rate of surface diffusion of ions, leading to sintering and crystal growth [42,43]. The γ - α phase transition occurs in alumina nanocrystalline compacts at temperatures $>1273 \text{ K}$,

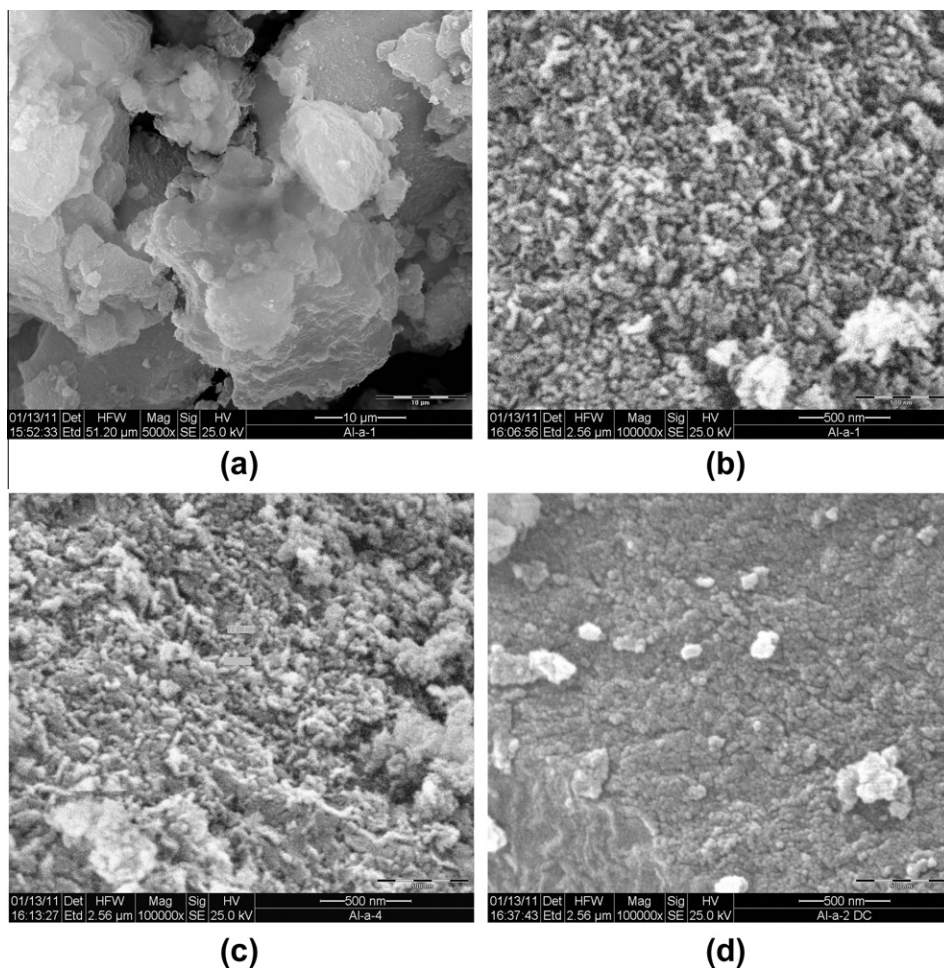


Fig. 2. SEM micrographs of starting alumina aerogel A-1073-2 (a and b) and the same aerogel after thermal (A-1073-14) (c) and chemical (ACD-1073-2) (d) densifications.

while densification starts at 1073 K [37,38]. Therefore, the XRD characterizations of all samples treated at 1073 K independent of the exposure time (Fig. 1) did not show the appearance of any amount of alpha-alumina phase. Another technique, which has been successfully implemented for densification of a MgO catalyst, is “chemical densification” [29]. In this technology, which resembles ceramics slit casting [39], the mesopores of the nanocrystalline oxide compact are filled with additional nanocrystals of the same material, and the precursor of the required oxide phase (hydroxide) is formed as a result of a chemical reaction inside the pores. Thermal treatment of the material results in crystallization of the required phase. The chemical densification increases the contact interface of the primary particles, thereby favoring the formation of GB areas with stabilized atomic disorder [29].

In the present work, increasing the nanocrystals’ contact interface of the reference alumina aerogel was achieved by both thermal and chemical densification. The former was conducted by heating the material in an oven in the atmosphere at a temperature of 1073 K for 4, 8, or 12 h to produce samples A-1073-6, A-1073-10, and A-1073-14, respectively. As the calcination time was increased, the surface area decreased from 498 m² g⁻¹ in the reference aerogel to 198 m² g⁻¹. The total pore volume decreased from 3.5 to 1.4 cm³ g⁻¹ (Table 1). The mesopore size distribution did not change in response to heating for 4 and 8 h, but after 12 h, the PSD maximum was shifted to lower pore size (Fig. 4b). The size of primary nanocrystals of γ -Al₂O₃ increased slightly from 2 to 2.5 nm after heating the reference aerogel for 4 h, as reflected by a contraction of the XRD reflections (Fig. 1, curves 2 and 3),

remaining unchanged up to 12 h (Fig. 1, curves 3–5; Table 1). The micropore volume decreased gradually by a factor of 5 after 12 h of heating. The micropore surface area demonstrated a similar trend (Table 1). These findings indicate efficient densification of the intermediate particles (the agglomerates of the primary nanocrystals). Further heating of the A-1073-2 material at 1073 K for 18 h caused visible sintering of primary crystals, thereby increasing their size to 3–3.5 nm without decreasing the total surface area. Coarsening of the agglomerates (the intermediate particles) occurred due to nonuniform grain growth in areas with different extents of densification which created micropores between the primary nanocrystals (Table 1). The consequent decrease in the value of aggregation ratio Ψ to 2.3 is due to the reduced nanocrystal interface.

The SEM study revealed significant shrinkage of the intermediate nanoparticles resulting in the building of large micron-size particles of the material powder. After heating the reference aerogel for 12 h, the size of these intermediate nanoparticles decreased from 25–100 to 15–70 nm, with a slight decrease in the size of the voids between them (Fig. 2b and c), which is consistent with the minor shift of pore size distribution (shown in Fig. 4b). Shrinkage of the primary nanocrystal aggregates together with the reduction in micropore volume/surface area in the material reflects the efficient densification of the intermediate nanoparticles, as was further confirmed by HRTEM. The HRTEM micrograph of such an aggregate of primary nanoparticles in sample A-1073-14 heated for 12 h did not show the slit-shaped voids (Fig. 3b and inset) that clearly divided the primary nanocrystals in the starting reference

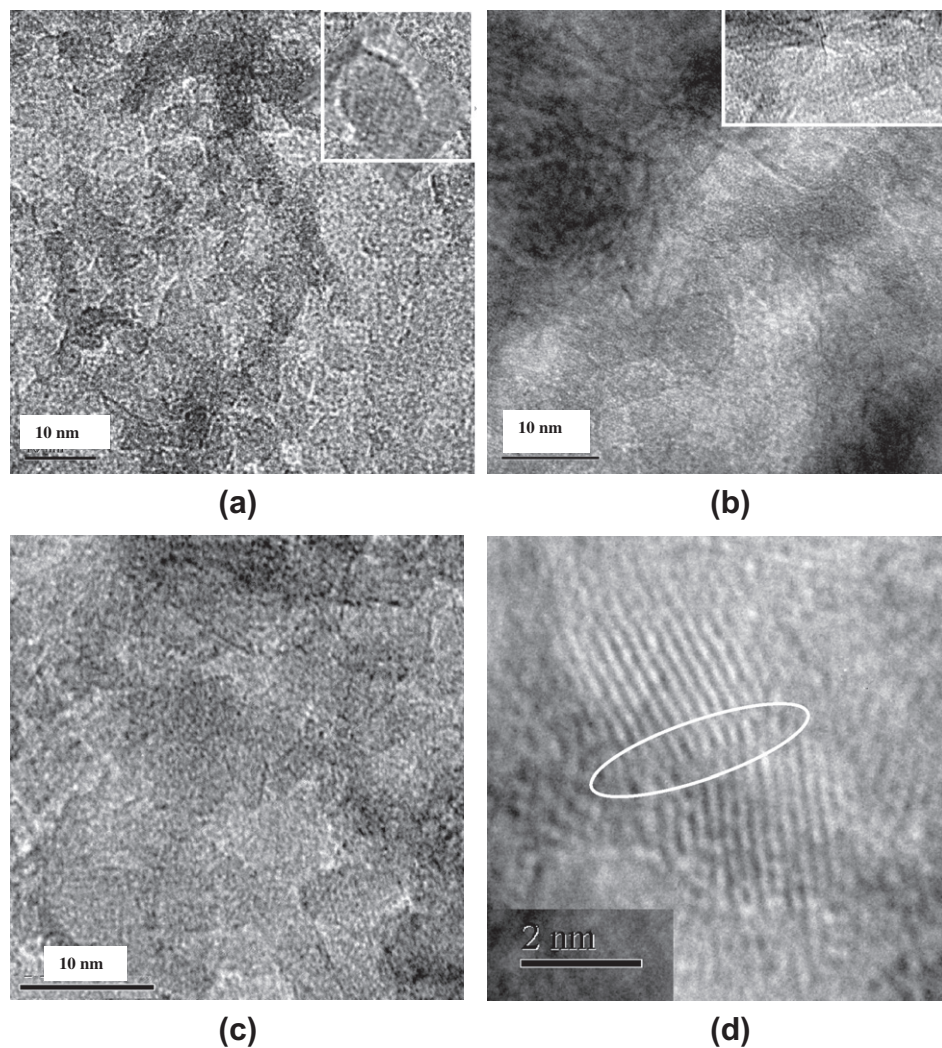


Fig. 3. HRTEM micrographs of γ -alumina derived from alumina aerogel: (a) A-1073-2; (b and d) A-1073-14; (c) ACD-1073-2.

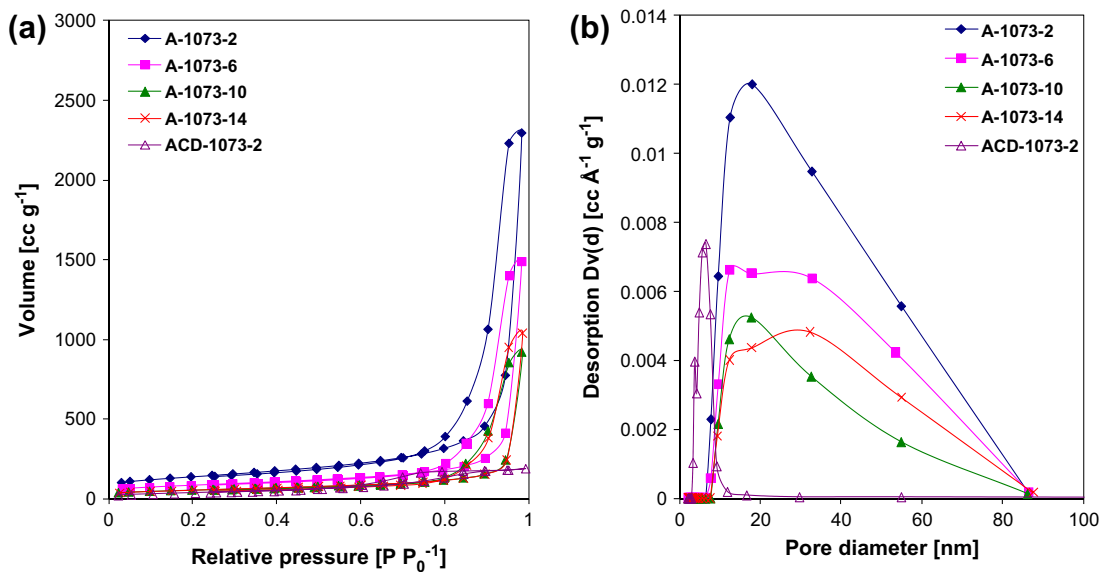


Fig. 4. N_2 adsorption-desorption isotherms of reference and densified alumina aerogels (a) and pore size distributions derived from the desorption branch of isotherms (b).

Table 1
Characterization of reference and densified aerogels.

Sample No.	γ -Al ₂ O ₃ materials	Total S.A. _{BET} (m ² g ⁻¹)	Micro S.A. (m ² g ⁻¹)	Total P.V. (cc g ⁻¹)	Micro P.V. (cc g ⁻¹) × 10 ²	Crystal size (nm)	Crystals aggregation ratio Ψ	Total acidity (mmol g ⁻¹)
1	A-1073-2	498	43	3.5	1.9	2	1.7	1.3
2	A-1073-6	324	31	2.3	1.4	2.5	2.0	1.7
3	A-1073-10	205	23	1.4	1.0	2.5	3.2	2.0
4	A-1073-14	198	11	1.4	0.4	2.5	3.3	2.5
5	A-1073-20	205	25	0.9	1.1	3.5	2.3	1.7
6	ACD-1073-2	132	0	0.3	0.0	4	3.1	1.5

aerogel (Fig. 3a and inset). The lack of slit-shaped voids may be attributed to the thermally induced rearrangement in the assemblies of primary nanocrystals, which eliminated micropores attached to the GBs (reflecting the high GB mobility) [42,43]. The twofold increase in the aggregation ratio Ψ , from 1.7 to 3.3 (Table 1), is a quantitative measure of the densification of the nanocrystals assemblies, which yielded a proportional rise in the nanocrystals' interface. The significant decrease in the total pore volume detected by N₂ adsorption measurements (Table 1) can be attributed to the shrinkage of large micron-sized particles of the material powder, with a consequent reduction in mesopores.

The attempt to carry out the “chemical densification” of the reference alumina aerogel by insertion and gelation of an alumina sol inside its pores or pores of its AlOOH precursor, as for MgO [29], did not succeed. The dried AlOOH precursor was converted back to the gel, yielding, after supercritical drying and calcination, a material with characteristics similar to that of reference aerogel. Loading the calcined aerogel with alumina sol increased the primary γ -Al₂O₃ nanocrystals in the calcination step. The “chemical densification” was conducted by insertion of aluminum nitrate salt solution inside the pores of AlOOH oxide–hydroxide precursor of the reference aerogel, followed by thermal decomposition of this salt in He at 573 K and calcination in O₂ at 1073 K for 2 h. The simultaneous formation of nanocrystals of the γ -Al₂O₃ phase from two sources, aluminum nitrate and AlOOH, in the calcination steps yielded a material consisting of pure γ -Al₂O₃ with a crystal size of 4 nm (Fig. 1, curve 6; Table 1). That ACD-1073-2 material had narrow pore size distribution with a mesopore diameter of 6–7 nm, i.e., a diameter significantly lower than that of the reference and of the thermally densified aerogels (Fig. 4b), probably as a result of filling of the large 20- to 90-nm pores formed in the reference aerogel with agglomerates (compacts) of γ -Al₂O₃ nanocrystals.

The intermediate nanoparticles in the chemically densified alumina aerogel had globular shape and a narrow size distribution in the range of 20–40 nm; these nanoparticles were densely packed inside the powder particles (Fig. 2d). This finding was consistent with the uniform and smaller diameter mesopores and the low total pore volume of 0.3 cm³ g⁻¹ detected by N₂-adsorption. The ACD-1073-2 material displayed a surface area of 132 m² g⁻¹ and did not contain micropores (Table 1). As expected, voids dividing primary nanocrystals were not observed at HRTEM micrographs

of this material (Fig. 3c). The high value of aggregation ratio $\Psi = 3.1$, close to that of the thermally densified aerogel, even though the primary nanocrystals were much larger, indicates that the chemically densified aerogel consisted of completely densified intermediate nanoparticles.

It was expected that the intermediate particles creating the surface of the densified alumina aerogels would be enriched with low-coordinated aluminum ions located in the GB areas, which were characterized by atomic disorder relative to the nanocrystal bulk with highly ordered atomic layers. This disorder arises as a result of a mismatch of the atomic layers of nanocrystals at their contact interface, as is clearly visible in the HRTEM micrograph obtained at high magnification (Fig. 3d). The theory and practice of material science regards the interfacial defects such as the GB observed in the densified material as high-angle GBs as opposed to the low-angle GBs, known as dislocations, which are generally observed inside large monocrystals [44]. The formation of high-angle GBs as a result of densification of γ -alumina nanocrystal assemblies is illustrated schematically in Fig. 5.

The contribution of low-coordinated ions in the GB areas to the total amount of atoms is expected to increase with progressive densification. Creation of atomic disorder in densified materials was indeed reflected by the larger integral intensity of the amorphous halo in XRD patterns centered at $2\theta = 30^\circ$ moving from sample A-1073-2 to densified A-1073-14 and ACD-1073-2 (Fig. 1). From the XPS spectra recorded for samples of A-1073-2 (reference aerogel) and thermally densified A-1073-14, it is evident that densification led to a decrease in the surface O/Al ratio from 1.70 to 1.58, which may be a result of ionic surface-bulk redistribution creating at the surface coordinative unsaturated (CUS) aluminum ions. The Al2p spectra of the two samples presented in Fig. 6 displayed envelopes that included the high-energy and low-energy components typical of Al₂O₃ [45]. Densification increased the width of the low-energy peak by 0.2 eV and shifted its BE from 74.05 to 74.15 eV, while the BE of the high-energy peak attributed to coverage of the alumina surface with carbon was shifted from 75.4 to 75.55 eV. This may be as a result of increasing the charging of surface aluminum ions due to lower coordination.

The low-coordinated tetrahedral T_d aluminum ions responsible for Lewis acidity of γ -alumina [46,47] can be created and stabilized in GB areas in amounts proportional to the nanocrystal

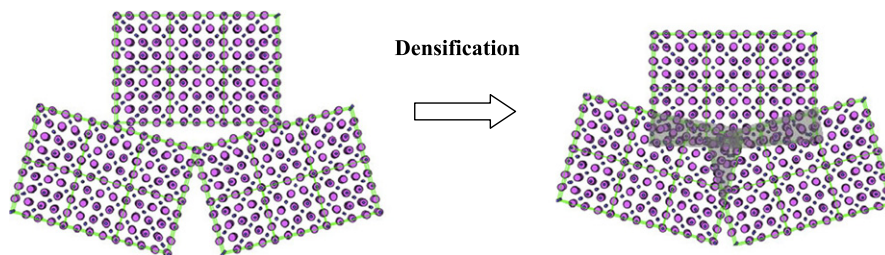
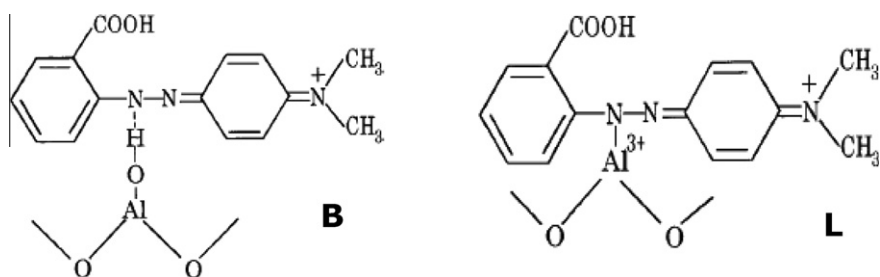


Fig. 5. Schematic representation of formation of GB areas during densification of nanocrystalline γ -alumina material.

interface. Formation of these ions as well as change in symmetry and in the environment of the tetrahedral and octahedral sites upon densification of alumina aerogel (by applying both thermal and chemical strategies) was confirmed by ^{27}Al MAS NMR measurements. ^{27}Al single-pulse magic angle spinning solid-state NMR spectra of the parent alumina (A-1073-2), thermally densified alumina (A-1073-14), and chemically densified alumina (ACD-1073-2) are shown in Fig. 7. The relative number of tetrahedral sites (T_d) was larger in the chemically and thermally treated species than in the parent material, with slightly more T_d sites in the chemically treated sample. Integration of the peaks yielded $16.0 \pm 0.3\%$ T_d sites for the parent alumina and $23.0\text{--}24.0 \pm 0.5\%$ of T_d sites for the chemically and thermally treated samples. The densified species also showed a broader distribution of both octahedral and tetrahedral sites, as can be seen from the line widths and line positions in the spectra. The shift in the center of the peaks corresponding to the T_d sites in the modified samples (68.7–68.9 ppm as compared to 74.8 ppm in parent alumina) may be attributed to an increase in their distortion, since the observed shift decreases as the quadrupolar coupling increases [48]. The obtained data give a strong basis to expect that the surface acidity of nanostructured γ -alumina together with other established factors as crystal size, thermal treatment, surface hydration–dehydration, and others [47,49–52] can be efficiently controlled also by adjusting the nanocrystals contact interface implementing variable densification strategies.

3.2. Surface acidity of reference and densified alumina aerogels

The surface acidity of the reference alumina aerogel, evaluated by titration, before and after thermal and chemical densifications, is given in Table 1. The chosen Hammett indicator – methyl red indicator ($\text{p}K_a$ 4.8) – is not selective for the type of acid sites; it converts to its basic state after adsorption at either Brønsted (B) or Lewis (L) acid sites on the alumina surface:



The figures given in Table 1 thus reflect the total (B + L) acidity for the sites with acid strength corresponding to the value of Hammett acidity function $H_0 \leq 4.8$. The total acidity normalized per gram of material rises gradually with increasing nanocrystal contact interface, as represented by the Ψ value, despite decreasing surface area (Table 1). This rise in acidity yielded a fivefold increase in the specific surface acidity normalized per 1 m^2 of material, in direct correlation with the increase in the nanocrystal aggregation ratio Ψ after thermal or chemical densification (Fig. 8, curve a). Sintering of nanocrystals after prolonged thermal treatment (18 h) caused a decrease in the Ψ value due to corrugation of nanocrystals' aggregates and appearance of micropores (sample A-1073-20). As a result, a significant decrease in the surface acidity both per gram and per 1 m^2 of material is in agreement with the decrease in the Ψ value (Table 1). Therefore, the observed increase in acidity upon densification of $\gamma\text{-Al}_2\text{O}_3$ nanocrystals aggregates can be attributed to the areas of atomic disorder that formed at

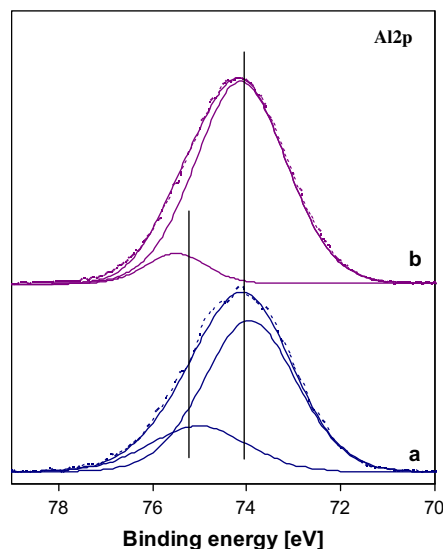


Fig. 6. XPS spectra of reference A-1073-2 (a) and densified A-1073-14 (b) alumina aerogels.

the intercrystalline GBs due to mismatching of atomic layers, as were clearly visible in the HRTEM micrograph (Fig. 3d).

Comparison of the FTIR spectra of adsorbed pyridine obtained for the reference and densified alumina aerogels showed that the increase in total acidity obtained by indicator titration was generated exclusively by the increase in the surface concentration of Lewis acid sites (Fig. 9 curves b–d, peak centered at 1450 cm^{-1} [53–55]), with no detectable change in the integral intensity of the peaks attributed to Brønsted acid sites (surface hydroxyls, $1490, 1540 \text{ cm}^{-1}$ [53,54]). The TPD spectra of preadsorbed NH_3 base (Fig. 10) were consistent with the results of indicator titration. Densification of the reference aerogel increased the surface acidity,

as reflected by the twofold rise in the corresponding TPD peak area. This finding was in agreement with the increase in surface acidity on a per weight basis by a factor of 1.9. The arising additional Lewis acid sites displayed the higher acid strength as ammonia was desorbed at $\sim 100 \text{ K}$ higher than from reference aerogel and characterized by increased area of high-temperature (800 K) peak (Fig. 10).

It was found that the increase in the surface concentration of acid sites after thermal and/or chemical densification of nanocrystal aggregates generated additional Lewis sites without the weight loss caused by surface dehydration/deoxygenation. The DTG spectra recorded for the hydroxide precursor of the reference alumina aerogel showed an envelope that included four peaks centered at 300, 650, 760, and 860 K (Fig. 11). These peaks were attributed to the removal of physically adsorbed water (300 K), dehydration–decomposition of bulk alumina oxide-hydroxide (500–800 K), and surface dehydration of the formed $\gamma\text{-Al}_2\text{O}_3$ phase (650–1050 K) [56–58]. Keeping the dehydrated reference aerogel (A-1073-2) at

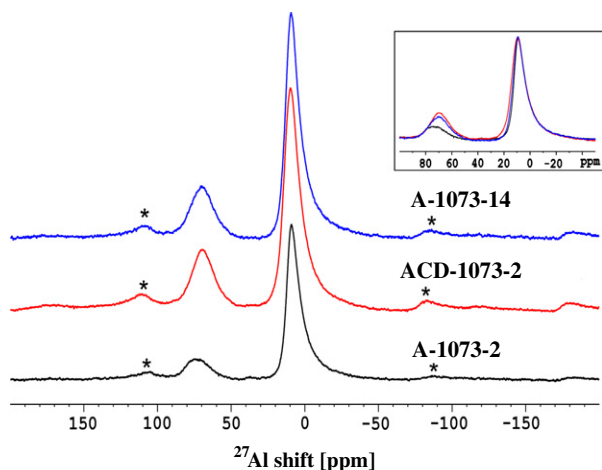


Fig. 7. ^{27}Al magic angle spinning solid-state NMR spectra. Bottom: A-1073-2, octahedral (O_h) site – 9.0 ppm, $84.0 \pm 1.7\%$; Tetrahedral (T_d) site – 74.8 ppm, $16.0 \pm 0.3\%$. Middle: ACD-1073-2: O_h – 9.7 ppm, $76.0 \pm 1.5\%$; T_d – 68.7 ppm, $24.0 \pm 0.5\%$. Top: A-1073-14: O_h – 9.5 ppm, $77.0 \pm 1.5\%$; T_d – 68.9 ppm, $23.0 \pm 0.5\%$. Asterisks denote spinning sidebands belonging to the satellite transitions of ^{27}Al (a spin-5/2).

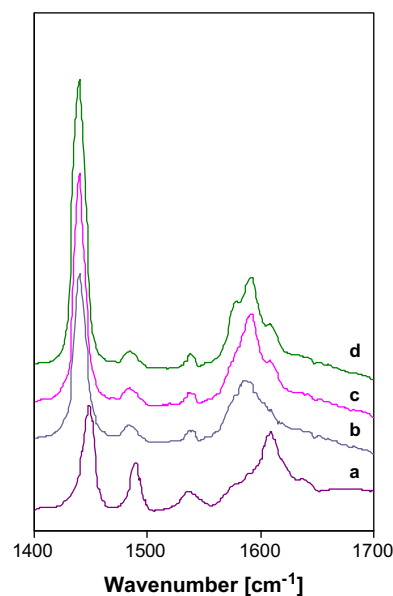


Fig. 9. FTIR spectra of pyridine chemisorbed on γ -alumina: (a) C3-823-2; (b) A-1073-2; (c) A-1073-10; (d) A-1073-14.

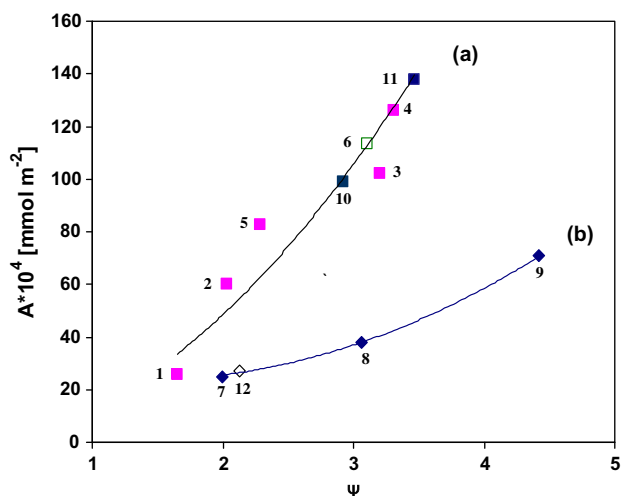


Fig. 8. Effect of aggregation ratio of γ - Al_2O_3 primary nanocrystals on their surface acidity: (a) aerogel; (b) xerogels and commercial alumina.

1073 K for an additional 12 h – a period during which intensive densification of the nanocrystal aggregates occurred – was accompanied by a marked rise in total acidity by 1.2 mmol g^{-1} (Table 1). The decrease in acidity after thermal treatment of the material at the same temperature of 1073 K extended to 17 h also did not change the samples weight (Fig. 11). These observations agree with the well-established results of alumina surface dehydration [49]. It was found that at high temperatures of 923–1173 K, the extent of surface dehydration related to the weight loss was governed mainly by the temperature, so that after increasing the temperature to the desired level, an additional water loss was observed at periods up to about 30 min.

Accepted models of Lewis acid sites at the surface of γ - Al_2O_3 attribute these sites to coordinatively unsaturated aluminum cations (CUS, low-coordinated surface ions), i.e., tri-coordinated into a tetrahedral site and penta-coordinated into an octahedral site, formed as a result of dehydroxylation of hydrated oxide surface – bulk-resembling or modified-amorphized crystallographic planes

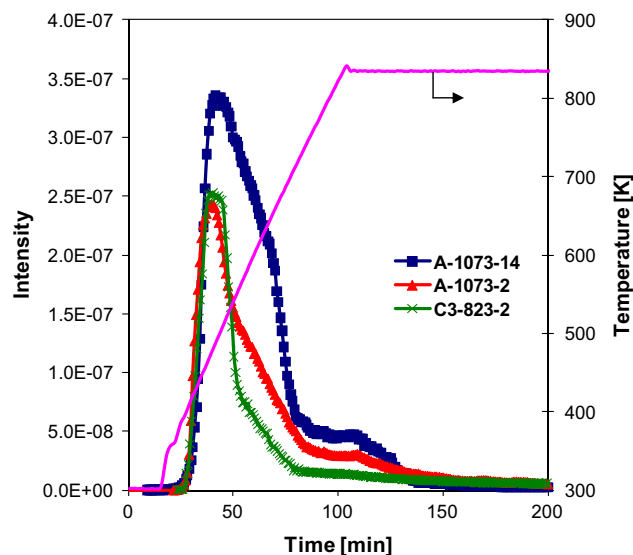


Fig. 10. NH_3 -TPD spectra of alumina aerogels and commercial alumina.

[46,47,49–52]. Conventional dehydroxylation starts from pairs of neighboring hydroxyls, leaving coordinatively unsaturated electron-deficient surface aluminum ions without rearrangement of the surface structure. Elimination of $>75\%$ surface hydroxyls requires rearrangement of oxygen ions and vacancies in the surface layers, while removal of $>90\%$ surface hydroxyls is possible only as a result of migration of ions along the surface. All these formation mechanisms of Lewis acid sites at the alumina surface assumes dehydroxylation: $2\text{Al-OH}^- \rightarrow \text{H}_2\text{O} + \text{AlO}^- + \text{Al}^+[\cdot]$, where $\text{Al}^+[\cdot]$ is a surface oxygen vacancy creating a low-coordinated (CUS) Lewis acid site. This scenario implies that the detected increase in surface acidity by 1.2 mmol g^{-1} after heating the reference aerogel for 12 h at 1073 K (Table 1) should give a loss of 1.2 mmol of water per gram of alumina, which is equivalent to a weight loss of 22 mg g^{-1}

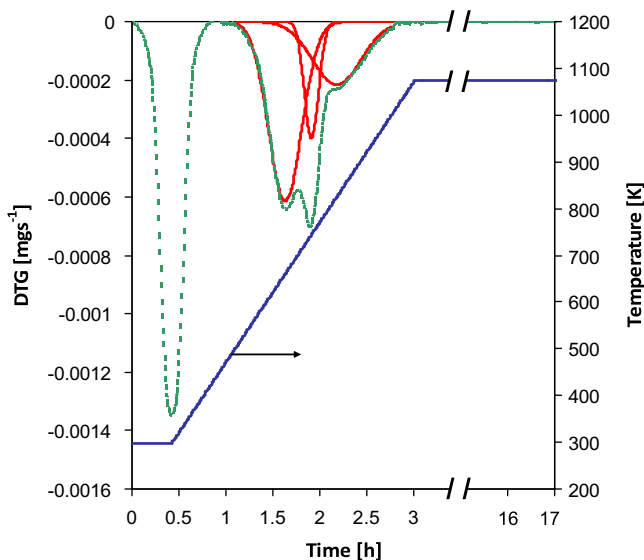


Fig. 11. DTG spectra of alumina aerogel precursor.

Al_2O_3 . For a sample weight of 20 mg as used in the TG measurements, this figure corresponds to an absolute weight loss of 0.44 mg, which should be clearly detected with the instrument used (having two orders of magnitude higher sensitivity of ± 0.001 mg). But TG analysis (Fig. 12) did not show any weight loss during that treatment period. The explanation for this finding lies in areas with atomic disorder at high-angle GBs, which after increasing the intercrystalline interface (densification) serve as an additional source of low-coordinated aluminum ions, i.e., Lewis acid sites. The contribution of this “non-dehydration” source to the total Lewis acidity of the alumina aerogel is comparable with that of the regular dehydration. Formation of GB increases the surface acidity by about twice on a material weight basis (A-1073-14) without any weight loss or change of Brønsted acidity (dehydration) compared with the material dehydrated at 1073 K (A-1073-2), despite a more than twofold decrease in the total surface area (Table 1). The difference became much more marked upon comparison of the surface acidity per 1 m^2 of the material, where it rose by a factor of 5 (Fig. 8). The decrease in surface acidity with a drop in the Ψ value without change in the surface area and without weight loss after extended thermal treatment (samples

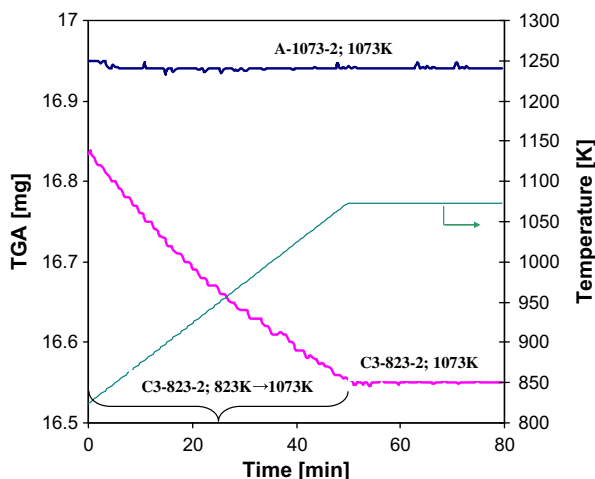


Fig. 12. TGA of reference alumina aerogel (A-1073-2) and commercial alumina (C3-823-2).

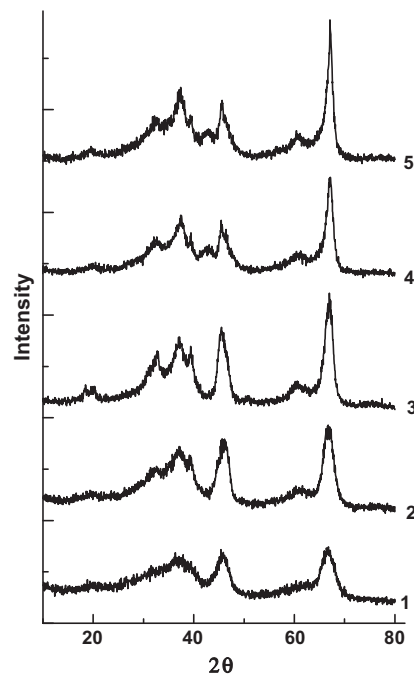


Fig. 13. X-ray diffraction patterns of γ -alumina material derived from xerogel: (1) X-823-3 and commercial aluminas: (2) C1-823-2 (Norton SA); (3) C2-823-2 (Norton XA); (4) C3-823-2 (Engelhard); (5) C3-1073-2.

A-1073-14 and A-1073-20, Table 1) constitutes direct evidence for the critical role of the nanocrystal interface. The formation of a contact interface is merely a precondition for the development of GB areas with atomic disorder. The latter appears as a result of counter-current diffusion of ionic pairs between neighboring oxide nanocrystals. The rise of surface acidity by 25% after 4 h heating of sample A-1073-10 (sample A-1073-14) without significant increase in the interface (aggregation ratio Ψ) reflects increasing the width of GB areas.

3.3. Densified aerogels and commercial aluminas: comparison of structure and surface acidity

Commercial aluminas from three different sources with unknown preparation histories and surface areas in range of 106 – $235 \text{ m}^2 \text{ g}^{-1}$ were compared with the densified aerogels prepared in the present work. For all the samples, the XRD patterns, shown in Fig. 13 (curves 2–4), indicated 100% crystallinity of cubic

Table 2
Characterization of commercial and xerogel derived γ -aluminas.

Sample No.	γ - Al_2O_3 materials	S.A. _{BET} ($\text{m}^2 \text{ g}^{-1}$)	P.V. (cc g^{-1})	Crystal size (nm)	Crystals aggregation ratio Ψ	Total acidity (mmol g^{-1})
<i>Commercial aluminas</i>						
7	C1-823-2	235	0.8	3.5	2.0	0.6
8	C2-823-2	153	0.8	3.5	3.1	0.6
9	C3-823-2	106	0.3	3.5	4.4	0.8
10	C3-1073-2	102	0.3	5.5	2.9	1.0
11	C3-1073-14	87	0.3	5.5	3.4	1.2
<i>Xerogel</i>						
12	X-823-2	257	0.5	3	2.1	0.7

γ -alumina (ICDD Card 79-1558). All the commercial aluminas consisted of nanocrystals with a similar average size of 3.5 nm. Their characteristics are listed in Table 2. The commercial aluminas displayed relatively high values of the nanocrystal aggregation ratio Ψ – similar or even higher (C3-823-2) than that of the values for the densified aerogels. Nonetheless, their surface acidity estimated on a weight basis was 3–5 times lower than that of the densified aerogels (Table 1). After normalization of the surface acidity per 1 m^2 , as in case of aerogels, the acidity of commercial materials increased with increasing nanocrystal aggregation ratio Ψ (Fig. 8, curve b), probably as a result of increasing the contribution to the total acidity of the acid sites generated in GB areas formed at the nanocrystal interfaces. For the commercial aluminas, however, the average rate of increase in surface acidity with increasing Ψ was 3.8 times lower: $(\partial A/\partial \Psi)_{\text{av.}} = 14.6$ ($A = 5.1034\Psi^2 - 14.159\Psi + 33.534$; Fig. 8, curve a) versus 55.1 ($A = 12.847\Psi^{1.918}$; Fig. 8, curve b) $\text{mmol}^{-4} \text{ m}^{-2}$ for aerogels, where A – specific surface acidity $\text{mmol}^{-4} \text{ m}^{-2}$ detected by titration. Both this finding and the significantly lower values of the surface acidity of the commercial aluminas estimated on both a weight and a surface area basis require further investigation.

The FTIR spectra of adsorbed pyridine (Fig. 9 curve a) showed that the surface acidity of commercial aluminas can be attributed to protonic Brønsted sites (intensive peaks centered at 1490 and 1540 cm^{-1}) as well as to Lewis acid sites. This finding is consistent with the results of the comparative TG analysis conducted with commercial alumina C3-823-2 pretreated at 823 K and with the reference aerogel calcined at 1073 K for 2 h (Fig. 12). The significant weight loss resulting from heating from 823 to 1073 K can be attributed to surface dehydroxylation (dehydration) of the commercial alumina. No weight loss was detected for the aerogel or the commercial alumina at 1073 K. According to the NH_3 -TPD spectra recorded for the reference (A-1073-2), densified (A-1073-14) aerogels, and commercial alumina C3-823-2 (Fig. 10), the concentration of strong acid sites retaining ammonia at temperatures $>650 \text{ K}$ is significantly lower in C3-823-2 sample compared with aerogels. The Brønsted acid sites at the alumina surface are weaker than Lewis acid sites produced by dehydroxylation [59]. Thus, the lower concentration of strong surface acid sites in the commercial alumina compared with aerogels can be attributed to the increased relative contribution of protonic acid sites to the total surface acidity in the former in agreement with FTIR data discussed above.

The lower rate of increase in the surface acidity of the commercial aluminas with the nanocrystal aggregation ratio Ψ can probably be attributed to different preparation methods. The calcination temperature of commercial aluminas was probably lower than that of the aerogels, as required for the complete crystallization of γ - Al_2O_3 by dehydration of pseudoboehmite [35,51]. This notion is consistent with the high extent of surface hydroxylation in the commercial materials observed in the FTIR spectra of adsorbed pyridine and in TGA spectra. The selected commercial aluminas are used mainly as catalysts supports where the high concentration and versatility of surface hydroxyls is of great importance [60].

For purposes of comparison, an alumina xerogel was prepared by precipitation of pseudoboehmite from an aqueous aluminum salt solution, followed by air drying and calcination at 823 K [35] (X-823-3). Its XRD patterns (Fig. 13, curve 1) and characteristics, listed in Table 2, including surface acidity and TGA spectra (not shown), were similar to those of commercial alumina. As expected, the value of surface acidity measured with this xerogel by indicator titration is similar to that of commercial alumina (Fig. 8, curve b, sample 10). Increasing Ψ stabilizes surface hydroxyls due to increasing distances between them at GB areas of atomic disorder. The lower (by 300 K) calcination temperature is probably the reason for the lower rate of increase in the surface acidity of commercial aluminas with nanocrystals aggregation ratio Ψ , vis-à-vis the

aerogel, due to the less efficient counter-current diffusion of ionic pairs through the intercrystalline contact interface, thereby making the GB areas narrower.

An attempt to increase the surface acidity of the most acidic commercial alumina C3-823-2, which did not contain micropores, by calcination at 1073 K for 2 h (as A-1073-14 aerogel) was not successful. Calcination yielded strong sintering of the primary nanocrystals of γ - Al_2O_3 (Fig. 13, curve 5), thereby increasing their size from 3.5 to 5.5 nm, without a significant decrease in the surface area (Table 2). As a result, the nanocrystal aggregation ratio Ψ decreased from 4.4 to 2.9, reflecting a strong drop in the intercrystalline interface. Therefore, despite efficient dehydroxylation of the material surface (as shown by TGA), the surface acidity of the C3-823-2 alumina did not increase significantly – only from 0.8 to 1.0 mmol g^{-1} (C3-1073-2, Table 2). Normalization of the acidity of the commercial alumina calcined at 1073 K (C3-1073-2) per 1 m^2 of the material yielded a value of $98 \times 10^{-4} \text{ mmol m}^{-2}$. This figure falls on the plot representing the dependence of the specific surface acidity of γ - Al_2O_3 aerogels on nanocrystal aggregation ratio Ψ (Fig. 8, curve a), and not on that for commercial aluminas and xerogel (Fig. 8, curve b). Extending the calcination of the commercial alumina C3-1073-2 at 1073 K for additional 12 h did not result in further sintering of the primary nanocrystals. Their average size remained at 5.5 nm, but the surface area dropped to $87 \text{ m}^2 \text{ g}^{-1}$ (C3-1073-14, Table 2). This decline of surface area, accompanied by an increase in the average pore diameter from 11 to 12 nm, can be attributed to aggregation of secondary nanocrystals assemblies, since the starting material did not contain micropores. This aggregation yielded a Ψ value of 3.4 and a further increase in surface acidity of C3-823-2 alumina to 1.2 mmol g^{-1} after extended calcination at 1073 K (C3-1073-14, Table 2). After normalization of the acidity of the C3-1073-14 material per 1 m^2 , the value of $137 \times 10^{-4} \text{ mmol m}^{-2}$ also falls on the plot representing the dependence of the specific surface acidity of γ - Al_2O_3 aerogels on nanocrystal aggregation ratio Ψ (Fig. 8, curve a). This finding further confirms the important role of the nanocrystal interface in the creation of surface acidity. In the preparation of alumina for applications as acidic catalytic materials, the intercrystalline interface, as one of the parameters significantly affecting the surface acidity, should thus be controlled carefully.

3.4. Catalytic activity of alumina in isopropanol dehydration: effect of densification

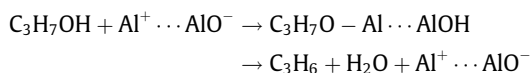
The catalytic materials prepared and characterized in this study were tested under standard conditions as catalysts in the dehydration of isopropanol. Isopropanol conversion is a test reaction for metal oxide catalysts, so that the direction of the reaction to dehydration (propylene) is catalyzed by surface acid sites, while hydrogenation to acetone is catalyzed by both acid and basic sites through a concerted mechanism [61]. The main product measured with all the aerogels was propylene, while the selectivity for diisopropylether did not exceed 5%. These findings may be taken as

Table 3

Effect of thermal and chemical densifications of Al-aerogel on its catalytic activity in isopropanol dehydration.

γ - Al_2O_3 materials	Ψ	Reaction Rate _w ($\text{mmol g}^{-1} \text{ h}^{-1}$)	Reaction Rate _s $\times 10^3$ ($\text{mmol m}^{-2} \text{ h}^{-1}$)	TOF (h^{-1})
A-1073-2	1.7	25	50	19.2
A-1073-6	2.0	30	110	17.6
ACD-1073-2	3.1	27	205	18.0
A-1073-14	3.3	43	220	17.2
C3-823-2	4.4	4	40	5.0

evidence for the acidic character of isopropanol conversion. The thermal densification increased the mass-related catalytic activity (reaction Rate_w) of the reference aerogel by >70%. The calculated surface reaction rates (reaction Rate_s) gradually increased with increasing nanocrystal aggregation ratio by a factor of 4.4, in good agreement with increasing surface acidity (Tables 1 and 3). The TOF calculated using surface concentrations of acid sites determined by indicator titration remained similar for all aerogels calcined at 1073 K. This finding reflects the similar reactivities and functionalities of Lewis acid sites formed via surface dehydration (A-1073-2) and via the “non-dehydration” route related to formation and expansion of intercrystalline high-angle GBs. These sites catalyze the dehydration of alcohols to the corresponding olefins through the formation of alkoxy intermediates after dissociation of molecules upon adsorption [54,61–64]:



The catalytic activity of the most acidic commercial alumina C3-823-2 (reaction Rate_w) was lower by an order of magnitude than that of the densified aerogel (see Table 3). The reason for it is a combination of lower surface acidity of commercial alumina C3-823-2 compared with densified material A-1073-14 (0.8 vs. 2.5 mmol g⁻¹) and different nature of surface acidity – higher contribution of protonic Brønsted acid sites and existence of basic surface hydroxyls in commercial alumina, reflected by lower TOF (5.0 vs. 17.2 h⁻¹). The latter was consistent with a decrease in the propylene selectivity measured with the C3-823-2 catalyst due to the production of acetone. Such behavior was also observed for aluminas calcined at the relatively low temperatures of 673–873 K [54]. It is well known that Lewis acid sites are significantly more efficient in isopropanol dehydration yielding higher TOF than hydroxyl groups at the alumina surface [53,62].

4. Conclusions

The alumina aerogel calcined at 1073 K has a hierarchical structure of small, 2–2.5 nm, near-globular primary nanocrystals of cubic $\gamma\text{-Al}_2\text{O}_3$ assembled in microporous secondary 25–100 nm nanoparticles that build the ternary mesoporous 1–50 μm powder. It was demonstrated that densification of the secondary nanocrystal assemblies by thermal treatment at 1073 K or by insertion of additional alumina into the material's pores yielded a fivefold increase in the specific Lewis surface acidity. The conclusion that this effect may be attributed to the creation of low-coordinated surface aluminum ions in the areas of high-angle GBs formed due to counter-current diffusion of ionic pairs through nanocrystals is based on the following specific findings:

- the shrinkage of secondary nanocrystal assemblies, with the disappearance of slit micropores, and atomic disorder at high-angle GBs as observed by N₂-adsorption, HRTEM, and XRD,
- the formation of low-coordinated aluminum ions with increased charging, as identified by ²⁷Al MAS NMR and XPS,
- the increase in acidity at 1073 K, not attributed to surface dehydration,
- the decrease in surface acidity due to sintering (grain growth) of primary nanocrystals, leading to coarsening of secondary nanocrystal assemblies and a decrease in the nanocrystal contact interface,
- the surface acidity of commercial alumina before and after dehydration depends on the nanocrystals' contact interface similar to alumina xerogel and aerogel, respectively.

Densification of secondary nanocrystal assemblies in the $\gamma\text{-Al}_2\text{O}_3$ aerogel increased the specific catalytic activity in isopropanol dehydration by a factor of 4.4; its mass-related activity was an order of magnitude higher than that of commercial alumina.

Acknowledgments

This study was supported by the Israel Science Foundation (Grant No. 739/06) and the Blechner Foundation. The authors gratefully acknowledge the help of Dr. A. Erenburg in conducting the XRD characterizations, Dr. N. Froumin for the characterization of alumina by XPS, and Professor N. Frage for the conceptual discussions.

References

- [1] M.-O. Coppens, G. Wang, in: U.S. Ozkan (Ed.), Design of heterogeneous catalysts: new approaches based on synthesis, characterization and modelling, Optimal Design of Hierarchically Structured Porous Catalysts, Wiley-VCH Verlag GmbH & Co. KGaA, Weinheim, 2009, pp. 25–58 (Chapter 2).
- [2] K.P. de Jong (Ed.), Synthesis of Solid Catalysts, Wiley-VCH Verlag GmbH & Co. KGaA, Weinheim, 2009.
- [3] G.R. Banwenda, S. Tsubota, T. Nakamura, M. Haruta, Catal. Lett. 44 (1997) 83.
- [4] J.J. Pietron, R.M. Stroud, D.R. Rolison, Nano Lett. 2 (2002) 345.
- [5] K.-W. Jun, H.-S. Roh, K.V.R. Chary, Catal. Surv. Asia 11 (2007) 97.
- [6] S.R.G. Carrazan, L. Cadus, Ph. Dieu, P. Ruiz, B. Delmon, Catal. Today 32 (1996) 311.
- [7] F. Su, F.Y. Lee, L. Lv, J. Liu, X.N. Tian, X.S. Zhao, Adv. Funct. Mater. 17 (2007) 1926.
- [8] D. Tsiplakides, S. Balomenou, Catal. Today. 146 (2009) 312.
- [9] W. Göpel, K.D. Schierbaum, Sens. Actuators B 26–27 (1995) 1.
- [10] D.S. Vlachos, C.A. Papadopoulos, J.N. Avaritsiotis, Sens. Actuators B 44 (1997) 458.
- [11] K. Hayek, M. Fuchs, B. Klötzer, W. Reichl, G. Rupprechter, Top. Catal. 13 (2000) 55.
- [12] Q. Fu, T. Wagner, Surf. Sci. Rep. 62 (2007) 431.
- [13] R.A. Van Santen, M. Neurock, Molecular Heterogeneous Catalysis; Conceptual and Computational Approach, Wiley-VCH, Weinheim, 2006 (Chapters 2 and 5).
- [14] M.I. Molotskii, Kinet. Catal. 15 (1974) 758.
- [15] Y. Yan, M.F. Chisholm, G. Duscher, A. Maiti, S.J. Pennycook, S.T. Pantelides, Phys. Rev. Lett. 81 (1998) 3675.
- [16] N. Gao, C.-C. Fu, M. Samaras, R. Schäublin, M. Victoria, W. Hoffelner, J. Nucl. Mater. 385 (2009) 262.
- [17] M. Yoshiya, H. Yoshizu, Mater. Trans. 51 (2010) 51.
- [18] S. Wen, Q. Liu, Microsc. Res. Technol. 40 (1998) 177.
- [19] H. Ichinose, Sci. Technol. Adv. Mater. 1 (2000) 11.
- [20] Y. Pang, P. Wynblatt, J. Am. Ceram. Soc. 88 (2005) 2286.
- [21] Y. Sato, T. Yamamoto, Y. Ikuhara, J. Am. Ceram. Soc. 90 (2007) 337.
- [22] S. Royer, D. Duprez, S. Kaliaguine, J. Catal. 234 (2005) 364.
- [23] S. Royer, D. Duprez, S. Kaliaguine, Catal. Today 112 (2006) 99.
- [24] J.S.J. Hargreaves, C.J. Hutchings, R.W. Joyner, C.J. Kiely, Catal. Today 10 (1991) 259.
- [25] J.S.J. Hargreaves, C.J. Hutchings, R.W. Joyner, C.J. Kiely, Catal. Today 13 (1992) 401.
- [26] J.S.J. Hargreaves, C.J. Hutchings, R.W. Joyner, C.J. Kiely, J. Catal. 135 (1992) 576.
- [27] S.V. Tsybulya, G.N. Kryukova, S.N. Goncharova, A.N. Shmakov, B.S. Bal'zhinimaev, J. Catal. 154 (1995) 194.
- [28] K.S. Kapolskii, P.J. Barczuk, S.Yu. Vassiliev, A.G. Veresov, G.A. Tsirlina, P.J. Kulesza, Electrochim. Acta 52 (2007) 7910.
- [29] R. Vidruk, M.V. Landau, M. Herskowitz, M. Talianker, N. Frage, V. Ezersky, N. Froumin, J. Catal. 263 (2009) 196.
- [30] S. Wen, J. Electron Microsc. Technol. 7 (1987) 301.
- [31] G. Kabalka, R.M. Pagni, Tetrahedron 53 (1997) 7999.
- [32] S. Tsuboi, Sci. Synth. 7 (2004) 247.
- [33] W. Turek, J. Haber, A. Krowiak, Appl. Surf. Sci. 252 (2005) 823.
- [34] D.J. Suh, T.-J. Park, J.-H. Kim, K.-L. Kim, Chem. Mater. 9 (1997) 1903.
- [35] B. Bloch, B.G. Ravi, R. Chaim, Mater. Lett. 42 (2000) 61.
- [36] M.A. Markowitz, P.E. Schoen, P. Kust, B.P. Gaber, Colloids Surf. A 150 (1999) 85.
- [37] C. Legros, C. Carry, P. Bowen, H. Hofmann, J. Eur. Ceram. Soc. 19 (1999) 1967.
- [38] C. Legros, F. Herbst, S. Lartigue-Korinek, C. Carry, P. Bowen, Rev. Metall. 99 (2002) 1073.
- [39] C. Tallon, M. Limacher, G.V. Franks, J. Eur. Ceram. Soc. 30 (2010) 2819.
- [40] M.N. Rahaman, Ceramic Processing and Sintering, Marcel Dekker, New York, 2003.
- [41] S.-J.L. Kang, Sintering, Densification, Grain Growth and Microstructure, Elsevier, Amsterdam, 2005.
- [42] R. Haim, M. Levin, A. Shlayer, C. Estournes, Adv. Appl. Ceram. 107 (2008) 159.
- [43] Z.Z. Fang, H. Wang, Int. Mater. Rev. 53 (2008) 326.
- [44] D. William, D. Callister, Materials Science and Engineering. An Introduction, John Wiley & Sons, New York, 2007.

- [45] I.V. Plyuto, A.P. Shpak, J. Stoch, L.F. Sharanda, Y.V. Plyuto, I.V. Babich, M. Makkee, J.A. Moulijn, *Surf. Interface Sci.* 38 (2006) 917.
- [46] A. Goldbourt, M.V. Landau, S. Vega, *J. Phys. Chem. B* 107 (2003) 724.
- [47] H. Knözinger, P. Ratnasamy, *Catal. Rev.-Sci. Eng.* 17 (1978) 31.
- [48] G. Engelhardt, H. Koller, *Magn. Reson. Chem.* 29 (1991) 941.
- [49] (a) J.B. Peri, R.B. Hannan, *J. Phys. Chem.* 64 (1960) 1526; (b) J.B. Peri, *J. Phys. Chem.* 69 (1965) 211; (c) J.B. Peri, *J. Phys. Chem.* 69 (1965) 220; (d) J.B. Peri, *J. Phys. Chem.* 69 (1965) 231.
- [50] C. Morterra, G. Magnacca, *Catal. Today* 27 (1996) 497.
- [51] P. Euzen, P. Raybaud, X. Krokidis, H. Toulhoat, J.-L. Le Loarer, J.-P. Jolivet, C. Froidefond, in: F. Schüth, K.S.W. Sing, J. Weitkamp (Eds.), *Handbook of Porous Solids*, Willey-VCH Verlag GmbH & Co. KGaA, Weinheim, 2002, pp. 1591–1677. vol.3.
- [52] G. Busca, *Chem. Rev.* 107 (2007) 5366.
- [53] M. May, J. Navarrete, M. Asomoza, R. Gomez, *J. Porous. Mater.* 14 (2007) 159.
- [54] J.A. Wang, X. Bokhimi, O. Novaro, T. Lopez, F. Tzompantzi, R. Gomez, J. Navarrete, M.E. Llanos, E. Lopez-Salinas, *J. Mol. Catal. A* 137 (1999) 239.
- [55] J. Sanchez-Valente, X. Bokhimi, F. Hernandez, *Langmuir* 19 (2003) 3583.
- [56] J. Lu, L. Gao, J. Guo, *J. Mater. Sci. Lett.* 20 (2001) 1873.
- [57] S.C. Shen, Q. Chen, P.S. Chow, G.H. Tan, X.T. Zeng, Z. Wang, R.B.H. Tan, *J. Phys. Chem. C* 111 (2007) 700.
- [58] S. Hamdani, C. Longuet, J.-M. Lopez-Cuesta, F. Ganachaud, *Polym. Degrad. Stab.* 95 (2010) 1911.
- [59] B.C. Lippens, J.J. Steggerda, in: B.G. Linsen (Ed.), *Physical and Chemical Aspects of Adsorbents and Catalysts*, Academic Press, London and NY, 1970, pp. 171–211.
- [60] J.-F. Lambert, M. Che, *J. Mol. Catal. A* 162 (2000) 5.
- [61] A. Gervasini, A. Auroux, *J. Catal.* 131 (1991) 190.
- [62] V.Yu. Borovkov, V.B. Kazanskii, *Kinet. Catal.* 15 (1974) 627.
- [63] J.M. Parera, N.S. Figoli, *J. Catal.* 14 (1969) 303.
- [64] V. Moravek, M. Kraus, *J. Catal.* 87 (1984) 452.